Nanoscale

Accepted Manuscript

This article can be cited before page numbers have been issued, to do this please use: M. A. Khan, M. Mujahid, J. Loo and V. C. Narasimhan, *Nanoscale*, 2020, DOI: 10.1039/D0NR01151G.

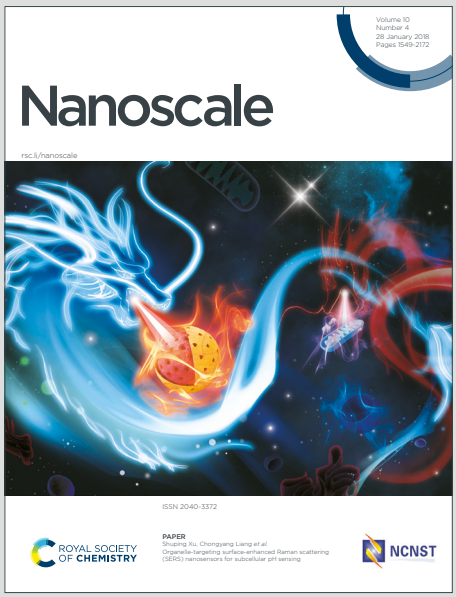

ROYAL SOCIETY OF CHEMISTRY

rsc.li/nanoscale

View Article Online
DOI: 10.1039/D0NR01151G

Nanoscale

PAPER

View Article Online
View Journal | View Issue

Cite this: DOI: 10.1039/xxxxxxxxxx

Nanophotonics based label free detection mechanism for real-time monitoring of interleukin-6†

Munezza A. Khan,*[a] Mohammad Mujahid,[b‡], Say Chye Joachim Loo[a] and Vidya N. Chamundeswari[a]

Received Date
Accepted Date

DOI: 10.1039/xxxxxxxxxx

www.rsc.org/journalname

Magneto-photonic crystals/MPCs are promising candidates for devising high-fidelity embedded biosensor system which offers facile & real time detection of diagnostic proteins. Despite of extensive use of magnetic nanomaterials for theranostic applications, the idea of exploiting its photonic response when assembled as colloid inside a matrix remained unexplored. Herein, we report a novel label free method for quantitative detection of Interleukin 6 which is a widely used prognostic marker for multiple pathological conditions. Cobalt Ferrite/CoF and magnetite nanoparticles with M_s of 74.8 and 77 emu/g were assembled inside a hydrogel matrix with the application of an external magnetic field. Through the use of click chemistry, detecting antibodies were immobilized on their surface. The interaction of interleukin 6 with antibody, produces a blue-shift in resonant wavelength and the reflectance intensity increases up to 50 % and 44 % when tested with CoF & Magnetite based MPC respectively at a concentration of 50 pg/ml. The dynamic range of sensor lies within the prognostic values of IL-6 and the integrated sensing mechanism proposed in this study, provides an ideal platform for real-time management of sepsis in patients with higher degree burns.

1 Introduction

The peculiar light emitting properties of certain organic & biological molecules have long been exploited for the development of fluorescence based Enzyme linked immunosorbent assay (ELISA) for detection of proteins which are of clinical significance. It involves a sandwich configuration of detecting and capturing antibodies which are used to bind with analyte and label respectively. It is a well-established and commercial method for quantitative analysis of diagnostic proteins. The complex multistep reactions and longer incubation time [1–3] prevent its application in *in-situ* real-time measurement which is an essential requirement of modern integrated health-care monitoring systems. The use of fluorophores as label, is an unattractive approach because signal reliability is compromised due to the photobleaching effect.

Label free technologies were introduced to obviate the need for fluorophores and shorten the incubation period [4–8]. The detection mechanism of the label free approach is either electrochemical or photo-electrochemical for an indirect competitive analyte binding immunoassay [7,9]. The electrochemical sensor's architecture provides wider dynamic range for detection of analyte with ultra-sensitivity compared to optical fluorescence based biosensors. It also eliminates the autofluorescence and photobleaching effects which decrease the accuracy of readout signal. A dual signal amplification strategy was introduced by Lou *et al.* and he used electro-active nanoparticles for electrode modification and competitor binding to enhance the charge transfer kinetics which ultimately amplify the output signal [9]. In contrast, Fan *et al.* used co-sensitized structure made of semi-conducting nanoparticles with stepwise band edge-gap for photo-electrochemical detection of interleukin 6 [7]. Despite of the high accuracy, ultra-sensitivity and wider dynamic range, the aforementioned sensor's structure cannot be used for the development of point-of-care (POC) devices due to multistep reactions and longer incubation time. Modern health-care system is more focused on the use of portable POC devices because it permits mobile patient monitoring.

Interleukin 6 (IL-6) is a multifunctional cytokine which is mainly involved in modulating immune response and hematopoiesis in human [10]. An over-expression of IL-6 in human body, is an indicative of multiple pathological conditions for instance cancer, lymphoma & sepsis [11–13]. Real-time monitoring of IL-6 levels in a patient will allow timely diagnosis and tracking progress of cancer remission. Herein we report a novel embed-

[a] *School of Materials Science & Engineering, Nanyang Technological University, Nanyang Avenue, Nanyanf Avenue, 639798, Singapore. Tel: +65 989 11907; E-mail: n1805860d@e.ntu.edu.sg*
[b] *School of Chemical and Materials Engineering, National University of Sciences and Technology, H-12, 44000, Islamabad, Pakistan.*
‡ Present address: Pak-Austria Fachhochshule, Institute of Applied Sciences & Technology, Khanpur Road, Mang, 22650, Pakistan
† Electronic Supplementary Information (ESI) available

View Article Online
DOI: 10.1039/D0NR01151G

ded sensing platform which can later be used for integration in portable POC based health care monitoring systems.

A paradigm shift in the transduction model for biosensing applications, is witnessed with the advent of sub-wavelength photonic crystal which exhibits tunable optical properties spanning across entire visible region [14,15]. Materials with varying dielectric constants when arranged periodically generate a photonic crystal, which has a photonic bandgap depending on its lattice constant [16]. The advancements in nanofabrication technologies over the past few decades have enabled researchers to develop intricate geometries with sub-wavelength spacings that produce resonant wavelengths. This makes them promising candidates for designing integrated biosensors [17,18]. Nanophotonics when combined with supramolecular chemistry allow us to design sensor's architecture which in response to biorecognition events generates either a shift in resonant wavelength or a change in refractive index [14,15,19].

Magnetic nanoparticles have been extensively investigated for drug delivery and magnetic resonance imaging (MRI) application due to their exquisite magnetic properties [20]. However, magneto-photonic crystal (MPC) for designing integrated biosensors have not been explored much. Inspired by the MPC developed by Ge *et al.* [21] that has size-dependent color tunable properties, we envisaged to fabricate a colloidal MPC for detection of Interleukin 6. Chitosan-gelatin hydrogel was selected as a supporting matrix for the formation of magneto-photonic crystal. The binding affinity of detecting molecules on sensor's surface increases when hydrogels are used as supporting matrix and it offers high sensitivity and signal-to-noise (S/N) ratio due to the increased immobilization efficiency [13,14]. Herein, we report MPC made of magnetite and Cobalt Ferrite (CoF) nanoparticles embedded in chitosan-gelatin matrix and compare their efficiency in quantitative detection of IL-6 through reflectance spectroscopy. Results are further confirmed by cyclic voltammetry method. We anticipate that such MPC based sensor platforms opens up avenue for devising next generation theranostic point-of-care devices for real time management of burn injuries or cancer remission using IL-6 as a prognostic marker.

2 Experimental

2.1 Materials

Gelatin (Type B; bloom 225), Chitosan (Degree of Deacetylation=75%; M_w=48.1KDa), Potassium Ferricyanide (M_w=329.25) were purchased from Daejung, Korea. Cobalt (II) Nitrate Hexahydrate was supplied by Scharlau, Spain. Iron (III) Nitrate Nonahydrate (Merck, Germany). Sodium Hydroxide (Fischer Chemicals Ltd). Dopamine Hydrochloride, Ammonium Hydroxide solution (28-30%), Iron (II) Chloride terahydrate, Cetyltrimethylammonium Bromide/CTAB (>98% purity), Iron (III) Chloride Hexahydrate & Aceton supplied by Sigma Aldrich. N-(-3-Dimethylaminopropyl)-N-ethylcarbodiimide hydrochloride (EDC) (98.5%; M_w= 191.7), N-hydroxysuccinimide 98%; M_w=115.09, Tris(hydroxymethyl)-aminomethane (99.8% pure; M_w=121.14) Buffer, Phosphate Buffer Saline (PBS), Ethanolamine (99% pure; M_w=61.08) were purchased from MACKLIN. 0.1M 2-(*N*-morpholino)-ethanesulfonic acid (MES) with 0.9% NaCl; pH4.7) purchased from Thermo Scientific. Interleukin-6 and Anti-interleukin-6 were supplied by Sigma Aldrich. PrestoBlue (Invitrogen), TrypLE, Fetal Bovine Serum (FBS) 10%, DMEM Media (Gibco, Life Technolgies), Penicillin & Streptomycin were supplied by Ionza. Human Dermal Fibroblast (HDF) were used for cell culture studies. Neodymium Block Magnets with dimensions $20 \times 10 \times 2$ mm were purchased from Titan Magnetics, Singapore.

2.2 Synthesis of Magnetic Nanoparticles/MNS.

Cobalt Ferrite and Superparamagnetic Iron oxide nanoparticles (SPIONS) were synthesized by using hydrothermal and co-precipitation methods mentioned in [22,23]. Protocols were followed without any modification and details of procedure can be obtained from the mentioned references.

2.3 Characterization.

Phase analysis and crystallite size of as-synthesized superparamagnetic Iron Oxide and Cobalt Ferrite nanoparticles were determined from XRD spectrum obtained using Powder X-ray diffractometer *(D8 Bruker Advance)* set in Bragg-Brentano ($\theta - 2\theta$) geometry. The step size was 0.1 and 2θ was scanned from 20° - 80°. The average size and morphology of nanoparticles were analyzed using Field Emission Scanning Electron Microscopy, *Nova NanoSEM 450*. Energy Dispersive X-ray Spectroscopy was performed to ensure absence of impurities in the prepared samples. Mass magnetization/M_s and coercivity were measured using Vibrating Sample Magnetometer, *Lakeshore 7400*. The maximum field applied to obtain M-H curve was 10 kOe.

2.4 Surface functionalization.

The magnetic nanospheres (MNS) were first functionalized with dopamine to augment immobilization efficiency of detecting antibody. We adopted the method defined in [24] and reacted dopamine Hydrochloride with MNS in a ratio of 1:50. First a stable dispersion was prepared by suspending 25mg of MNS in 25 ml of distilled water using ultrasonication probe (Labsonic M, Sartorius Stedim, Germany) set at a frequency of 1.6kHz. Dopamine HCl weighing 5 gm was later added in the suspension and the reaction vessel was left in bath sonicator (frequency 37kHz) for 45 minutes. Once the reaction time was over, unreacted dopamine was removed by washing MNS with acetone thrice. Later, it was lypholized and stored at 4 °C.

2.5 Bioconjugation of MNS with Detecting Antibody.

The as-synthesized MNS of Cobalt Ferrite and magnetite were bioconjugated with Anti-Interleukin 6 through EDC-NHS click chemistry reaction with a coating concentration of 125 μg/g. MNS weighing 2.5 mg was washed twice and suspended in MES activating buffer using bath sonicator. MES (25 μL) was also added in the Anti-IL 6 vial. Milli-Q ultrapure water for the preparation of buffer solutions and reaction mixture. The carboxyl groups on Anti-IL6 were activated by adding 0.2 M of EDC (9.6 μL) and

View Article Online
DOI: 10.1039/D0NR01151G

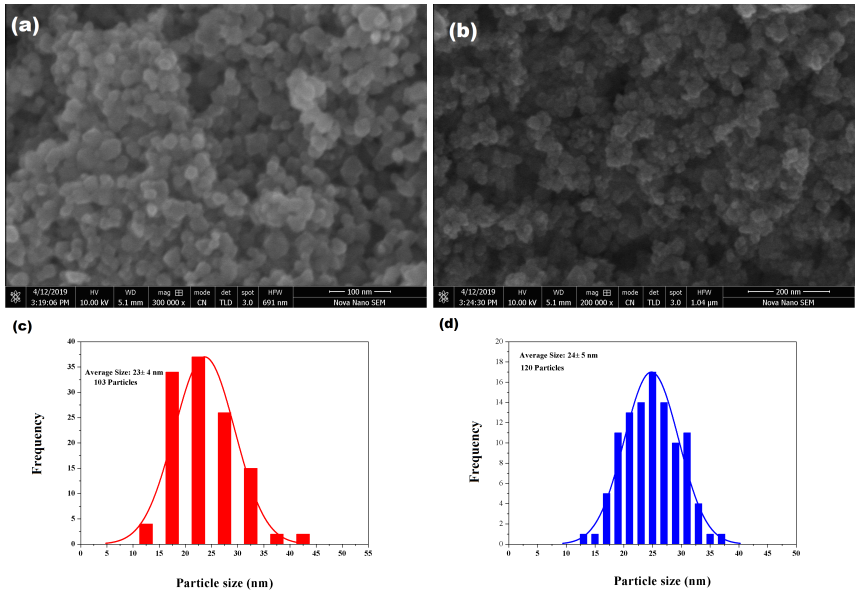

Fig. 1 Morphology and Size Distribution. (a) Scanning electron micrograph of CoF nanospheres. (b) Scanning electron micrograph of magnetite. (c) Size distribution of CoF MNS calculated from SEM micrographs with an average diameter 23±4 nm. (d) Magnetite size distribution plot calculated form SEM micrographs. The as-synthesized nanoparticles display a narrow dispersity as shown here while the average diameter of MNS is 24±5.

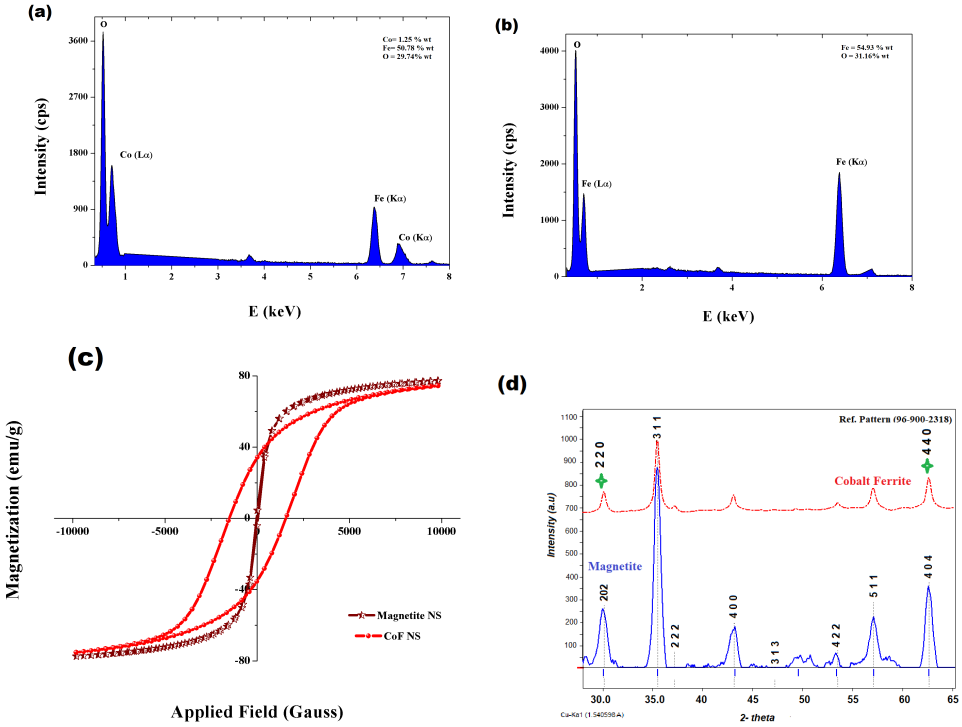

Fig. 2 Phase Purity & Magnetic properties. EDX spectra of (a) cobalt Ferrite & (b) Magnetite nanospheres (c) M-H curve of Cobalt Ferrite & Magnetite nanospheres demonstrating formation of superparamagnetic Iron oxide phase however the former displays hysteresis of 1532 Gauss (d) X-ray diffraction spectra of as-synthesized CoF and Magnetite nanospheres analyzed with reference patter 96-900-2318.

View Article Online
DOI: 10.1039/D0NR01151G

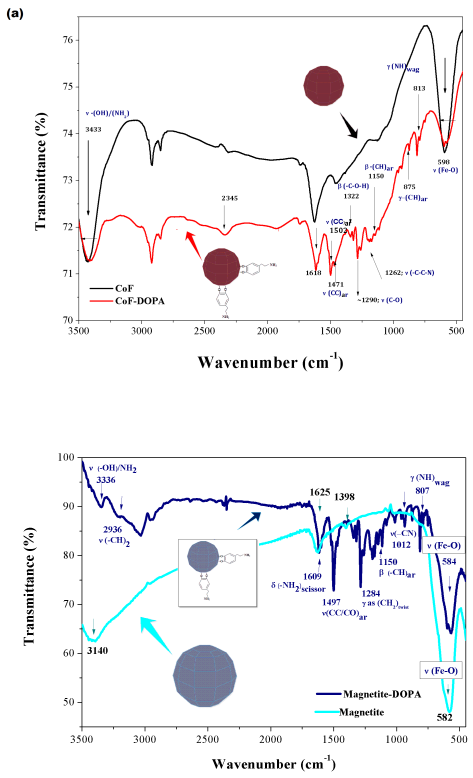

Fig. 3 Biofunctionalization of Magnetic Nanospheres.. (a) FTIR spectra of CoF MNS & (b) magnetite MNS functionalized with dopamine.

0.3M NHS (96 μL) and left for incubation on rotary wheel for 30 mins. In the mixture of activated anti-IL 6, we added 1 mL of already prepared MNS suspension. It was pipette mixed and later incubated on rotary wheel for 2.5 hours. Following this, the reaction was stopped by adding 50μL of ethanolamine in the reaction mixture and incubated for another 30 mins. Later, it was centrifuged at 7000 rpm for 7 mins. Supernatant was decanted and pellet of MNS was resuspended in Tris Buffer using bath sonicator (kept with dry ice for 10 mins). Tris-buffer was used as blocking buffer and the suspension was incubated for 1.5 hr. The bioconjugated MNS were washed thrice with Tris-buffer, suspended in PBS and stored at 4 °C.

2.6 Fabrication of MPC based Immunosensor.

MPCs were prepared by suspending bioconjugated MNS in Milli-Q water. The stable suspension was added in already prepared 1.5% chitosan (dissolved in 1% acetone solution) & 7% gelatin solutions. The concentration of bioconjugated MNS used for MPC preparation was 1.3mg/ml. The solution was probe sonicated for 5 mins and then 1 ml of it was drop casted on glass substrate. Magnetic field was applied using Neodymium (N38) Magnet (1×2cm) for a minute at a distance of 3 cm from slide to align MNS in one direction. Later, it was left for overnight curing in UV-light.

2.7 Electrochemical Measurements.

Cyclic voltammetry was performed to confirm antibody immobilization on the surface of magnetic nanospheres (MNS). Working electrode was prepared using method mentioned in our previous study[23]. Glassy carbon electrode with 3mm diameter was dip-coated in the colloidal suspension of bioconjugated MNS prepared in polymer solution. The electrode was cured overnight in UV light at room temperature. A three probe system was used for electrochemical measurement with Ag/AgCl saturated calomel and platinum wire as reference and counter electrode respectively. Working electrode was incubated for an hour in different concentrations of IL-6 (50, 150, 250 & 350 pg/ml) and then washed with PBS before placing in electrolytic cell to remove unbound antigen from the sensor's surface. We used 0.001M $K_3Fe(CN)_6$ as a redox probe and all measurements were performed at room temperature using potentiostat, *PARSTAT MC 1000*, AMETEK, US. Open Circuit voltage was set as initial potential and it was swept across +2 to -2 volts with scan rate of 0.05 V/s.

2.8 Reflectance Spectroscopy based Immunoassay.

First interleukin solutions with concentration of 50, 150, 250 & 350 pg/ml were prepared in PBS. We added 50 μL IL-6 solutions of mentioned concentrations on MPC coated glass slides. It was left on incubation at room temperature for an hour. Later, the slides were washed with PBS to remove unbound antigen and scanned at entire visible range using UV/Vis/NIR Spectrometer *(Lambda 950)*, Perkin Elmer to obtain their respective reflectance spectra.

3 Results & Discussion

3.1 Morphology & Magnetic Properties

Light diffracting properties of photonic crystal is precisely controlled by sub-wavelength spacing between Bragg reflectors. While designing magneto-photonic crystal, effective control over inter-particle spacing can be achieved by tuning size and shape of magnetic particles[25]. Certain ferromagnetic material when scaled down to few nanometers such that its grain size becomes identical to magnetic domain, align themselves in unison when external magnetic field is applied. This grain size is generally regarded as critical diameter/D_c. When the diameter of nanoparticles approaches closer to its D_c, transition from ferromagnetism to superpapramagnetism occurs. Cobalt Ferrite (CoF) and magnetite have D_c of 14 nm and 8 nm respectively[26,27]. Owing to their good biocompatibility and excellent magnetic properties, we found them promising candidates for fabrication of 3D colloidal magneto-photonic crystal for IL-6 detection. Magnetic nanopar-

Table 1 Structural and Magnetic Parameters of MNS

Type	Crystallite size †	Particle size †	D_c †	M_s ⋆
Cobalt Ferrite	9.7	23 ± 4	8	74.8
Magnetite	8.5	24 ± 5	14	77

† mentioned in nm; ⋆ mentioned in emu/g.

View Article Online
DOI: 10.1039/D0NR01151G

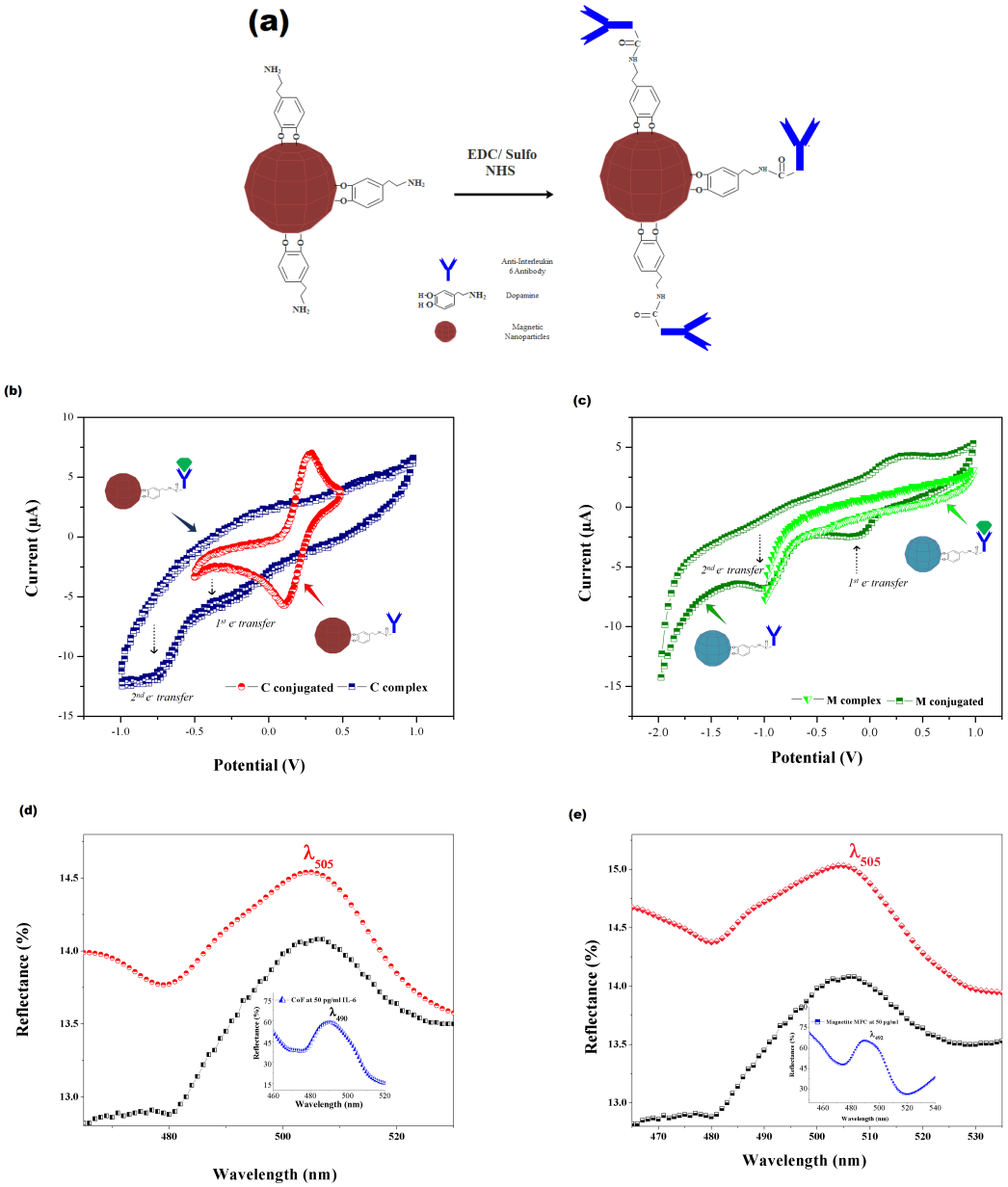

Fig. 4 Bioconjugation of Magnetic Nanospheres.. (a) Antibody against Interleukin-6 was conjugated with MNS through EDC/Sulfo-NHS click chemistry using dopamine as bifunctional coupling agent. (b) Cyclic voltammogram of CoF-MPC with & without IL-6 and Anti-IL 6 complex formation (c) Cyclic voltammogram of Magnetite-MPC with and without IL-6 & Anti-IL 6 complex formation recorded with E_{range} = -2.5 to +2.5 V; ν = 50 mV/s in 0.001M $K_3Fe(CN)_6$. (d) Reflectance spectra of CoF MPC unconjugated (black), conjugated with antibody (Red) and in complex with IL-6 at concentration of 50 pg/ml (inset plot in blue). (e) Reflectance spectra of Magnetite MPC unconjugated (black), conjugated with antibody (Pink) and in complex with IL-6 at concentration of 50 pg/ml (inset plot in blue).

ticles with size less than 100 nm & high saturation magnetization are assembled at stronger applied magnetic field and it ensures formation of a stable colloidal array[36]. Colloidal stability of magneto-photonic crystal based sensor brings improvement in signal-to-noise ratio and the readout signal is considerably amplified. Additionally, light diffracting properties of magneto-photonic crystal are size-dependent and $\leq$ 100 nm MNPs diffract blue light.

CoF magnetic nanospheres (MNS) were synthesized by hydrothermal method described in[23] using CTAB as surfactant which facilitated formation of cobalt Ferrite nanospheres with very narrow size distribution. As observed under scanning electron microscope, the average diameter of synthesized CoF nanospheres was 23±4 nm, refer to figure 1 a & c. The increased size of CoF MNS compared to its D_c resulted in hysteresis of 1532 Gauss when analyzed with vibrating sample magnetometer/VSM, Figure 2 c. In contrast, magnetite synthesized from co-precipitation method exhibits average diameter of 24±4 nm which is threefold greater than its D_c however the absence of hysteresis in magnetite MNS upon magnetization reversal indicates

View Article Online
DOI: 10.1039/D0NR01151G

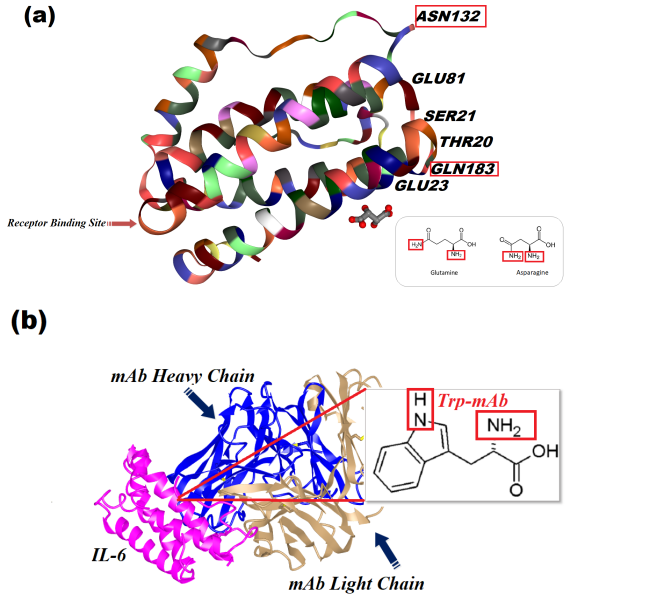

Fig. 5 Interleukin 6 and its complex with anti-interleukin 6 antibody. (a) Receptor binding site is present at D-loop while the free end at opposite site, possesses polar uncharged amino acids Asn, Gln which contain multiple amine groups in their structure[28]. (b) IL-6 complex with its antibody. Heavy chain of antibody contain Trp-169 which interacts with IL-6 and facilitate detection. Trp has one secondary and primary groups in its structure[29].

the formation of super-paramagnetic phase, see Figure 2 c.

The absence of chemical impurities was confirmed by energy dispersive x-ray spectroscopy. As indicated by EDX plot in figure 2 a & b, no undesirable ionic species were present in samples. Characteristic L_α & K_α of Co appeared at 0.776 and 6.924 keV respectively while only K_α of Fe was observed at 6.398 keV in magnetic nanospheres sample labeled Cobalt Ferrite. In magnetite, both peaks corresponding to L_α & K_α were obtained at 0.705 & 6.398 keV respectively. The XRD spectra demonstrate formation of single phase Magnetite and Cobalt Ferrite, the crystallite size was also determined using Scherrer's formula and mentioned in Table 1. All major peaks of magnetite phase matched with reference peaks (96-900-2318) however (313) peak is slighted shifted to higher angle. The appearance of (220) & (440) peaks in CoF MNS confirms the formation of single inverse spinel phase (Figure 2 d). It is worth noting that synthesized magnetite phase is well-suited for intended applications due to the predicted ease in magnetic alignment during the fabrication step of photonic crystal. For comparison, we also studied CoF MNS for development of magneto-photonic crystal and quantitative detection of IL-6.

3.2 Bioconjugation

The sensitivity of a biosensor is entirely dependent on the immobilization efficiency of capturing antibody on the sensor's surface. A careful selection of coupling agent is a widely used signal amplification strategy. We chose dopamine as a bifunctional coupling agent for the attachment of anti-IL 6 antibody on surface of magnetic nanospheres/MNS, refer to figure 4a. Dopamine has proven ability to augment outgoing electrical as well as optical readout signal when used as a linker due to the high affinity that biomolecules exhibit towards its terminal amino group[1,30–34]. The successful surface functionalization of MNS was confirmed through FTIR spectroscopy. Magnetite and Cobalt Ferrite interacts with amine group of dopamine through Fe-O bond. The decrease in intensity of Fe-O vibrations at 584 & 598 cm^{-1} of CoF and magnetite respectively along with the appearance of aromatic vibrations of -CC, -CO (at 1497; 1471 cm^{-1}) in the FTIR spectra, suggest dopamine reaction with as-synthesized MNS. A drastic drop in Fe-O stretch appears because octahedral Fe of CoF and Magnetite, interacts with -OH groups of dopamine in bidentate-bridging configuration[23]. The peaks at 813 and 807 (3 a & b) belong to $\delta(NH_2)_{scissor}$ of amine groups of dopamine while $\gamma-(NH)_{wag}$ vibrations at 1609 & 1618 in figure 3 a & b further confirm the presence of dopamine.

For electrochemical characterization to confirm bioconjugation, we dip-coated 3mm glassy carbon electrode (GCE) with hydrogel solution containing magnetic nanospheres and after overnight curing we recorded its cyclic voltammogram using $K_3Fe(CN)_6$ as redox probe (Supplementary figure 14 b & c). A comparison of cyclic voltammogram acquired with GCE modified with CoF and Magnetite MPC before and after incubation with IL-6 (at concentration of 350 pg/ml) is presented in Figure 4 b & c. Bioconjugated modified GCE shows a shift in formal potential/E_f from 0.45V to 0.2V when compared with CoF based magnetic nanogel reported in previous study[23], refer to figure 14a while the $\triangle E_p$ changes from -44mV to 187mV. Following attachment of antibodies, CoF based MPC illustrates unhindered reversible electron transfer kinetics at the interface however upon formation of antigen-antibody complex on the sensor's surface, electrode reaction shows transition to irreversible nature with two step electron transfer. The separation between two consecutive cathodic peaks is approximately ΔE° = - 590 mV. In contrast, Magnetite-MPC shows two well-spaced cathodic peaks with ΔE° =-850 mV that corroborate kinetically driven quasi-reversible electrode reaction prior to antigen binding process. The different response of the two MPC can be attributed to their inherent chemical reactivity with terminal amino or carboxyl groups present on the surface of proteins. However, a common observation in both types of MPC is the diminishing peak current with the formation of antigen-antibody complex which is rational due to the charge screening effect of double layer formed at electrode's interface. Interleukin 6 is a negatively charged protein and decrease in peak current is well justified as it increases the charge transfer resistance and repels negative redox species thereby decreases resulting peak current[34]. To understand the two step electron transfer process, we looked for the chemical species present on side chain amino acids of interleukin 6 and its antibody which can undergo step-wise reduction. Figure 5a demonstrates structure of IL-6 and its receptor binding site[35]. The protein structure contains four α-helices called A, B, C & D. D-loop contains -COOH groups which interact with antibody while the side chains at opposite end contain polar uncharged amino acids for instance Asparagine & Glutamine[28]. The two reductive peaks in CoF-MPC upon complex formation appear due to step-wise reduction of polar side chain amines such as Asparagine (Asn) and Glutamine (Gln),), refer to figure 5a and 4

View Article Online
DOI: 10.1039/D0NR01151G

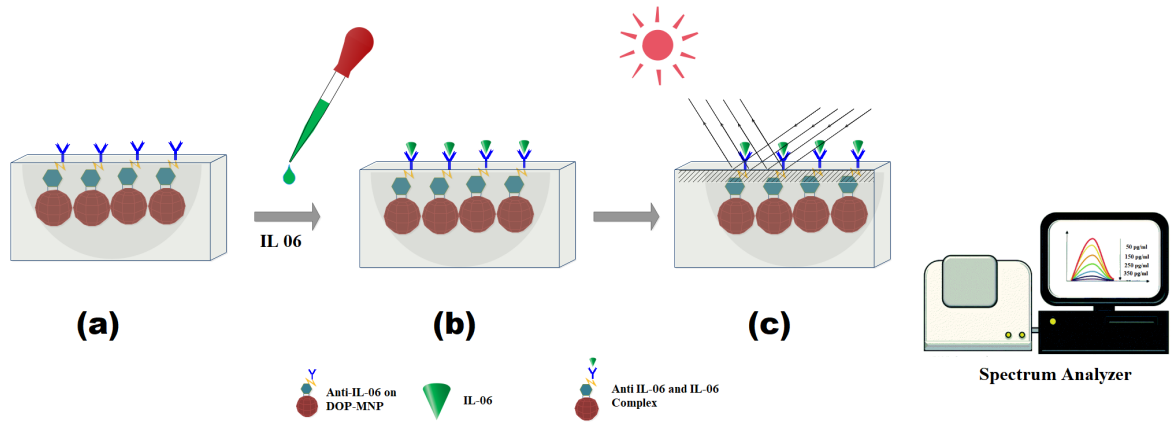

Fig. 6 MPC Reflectance Spectroscopy. (a) Magneto-photonic crystal assembled as 3D colloid inside chitosan-gelatin hydrogel. (b) Addition of IL-6 will result in the formation of antigen-antibody complex following an hour of incubation. (c) The bound complex on surface of MPC can be observed by illuminating it with visible light under spectrophotometer. The presence and varying concentration of IL-6 will produce a shift in λ_{Bragg} and reflectance intensity respectively.

b. In contrast, magnetite MPC shows quasi-reversible redox peaks prior to analyte binding because antibody binds to nanospheres through its carboxyl terminal at its Fc (constant region) region while the Fab (antibody binding region) fragment contains Tryptophan (Trp) residue which exhibits one primary and one secondary amine group, see figure 5b[29]. Quasi-reversible peak appears due to reduction of secondary amines and redox peak disappears upon complex formation because Trp is involved in IL-6 binding[29]. We can speculate that the peaks corresponding to Trp redox reaction in CoF-MPC sensor remain unresolved prior to antigen binding and appears as a single widely spaced reversible peak.

A comparison of reflection spectra obtained after bioconjugation and subsequent incubation with IL-6 at 50pg/ml, has been presented in Figure 4d and e. The inset graphs in figure 4d and e show reflection spectra of bound antigen-antibody complex. Binding of IL-6 to the bioconjugated MNS produces blue-shift in resonant wavelength/$\lambda_{505\rightarrow490/492}$ and the corresponding reflectance intensity increases. The *d*-parameter of colloidal crystal alters upon antigen-antibody complex formation which in turn causes shift in reflecting wavelength. MPC based immunoassay was performed *in-vitro* under physiological conditions (Temperature 37 °C ; pH 5-7.5). The aforementioned findings encouraged us to propose a novel magneto-photonic crystal based sensor for detection of IL-6 embedded in hydrogel which can be further modified for *in-situ* diagnosis of pathological conditions that demonstrate elevated levels of IL-6 for instance in sepsis and cancer[11,12].

3.3 Reflectance Spectroscopy & Electrochemistry

The schematic of immunoassay we designed for detection of IL-6 has been illustrated in Figure 6. In our previous work, we used colloidal assembly of CoF nanoparticles in combination with stimuli responsive hydrogel for controlled drug delivery applications[23]. A homogeneous dispersion was achieved inside the matrix when observed under scanning electron microscope. The intriguing light diffracting properties of magnetite based colloidal photonic crystal reported by Ge et al. motivated us to propose an integrated reflectance based detection mechanism for interleukin 6 through the use of a 3D colloidal MPC hydrogel[36].

The as-synthesized MPC hydrogel composed of CoF & Magnetite nanospheres, shows resonant wavelength at 505 nm represented by λ_{505} as discussed in previous section, figure 4 d & e. The diffracting resonant wavelength is dependent on the size of the magnetic nanospheres and below 100 nm, blue light is reflected[36]. In this study, Magnetite and Cobalt Ferrite nanospheres with average diameter of $\sim 24 \pm 5$ nm & $\sim 23 \pm 4$ nm were used so the observed resonant wavelength of fabricated MPC is well-justified, refer to figures 1 & 7 c & d. Quantitative detection of IL-6 was performed within a concentration range of 50-350 pg/ml. For reflectance spectroscopy analysis, we coated MPC hydrogels on glass slides and after overnight curing we incubated it with 50 μL of samples. Following an hour of incubation and after washing with PBS to remove unbound antigen, reflectance spectra were recorded. It can be observed from figure 7 c & d that analyte binding process produces a blue-shift in both types of MPC based hydrogel biosensors while intensity of reflecting wavelength changes in response to varying concentration of analyte (IL-6). Magnetite-MPC showed 50% increase in reflectance intensity upon IL-6 binding on its surface and the λ_{505} blue-shifted to λ_{492}, see figure 7 d. Only change in reflectance was observed in response to increasing concentrations of IL 6 while the λ_{492} remained constant. In contrast, CoF showed 44% increment in reflectance following IL-6 binding and the λ_{505} changed initially to λ_{491} and with increasing concentration of detecting analyte, it shows further right shift, refer to figure 7e.

To understand the electrochemistry of developed MPC based sensor's architecture, we performed CV analysis under conditions similar to the ones mentioned in previous section. Figure 7a demonstrates transition of reversible interfacial reaction to an irreversible two step electron transfer reaction. When the concentration of adsorbed interleukin 6 increases, the cathodic current changes and anodic peak diminishes while E_{pc} shifts to the left. Magnetite responds differently to the surface bound antibodies.

View Article Online
DOI: 10.1039/D0NR01151G

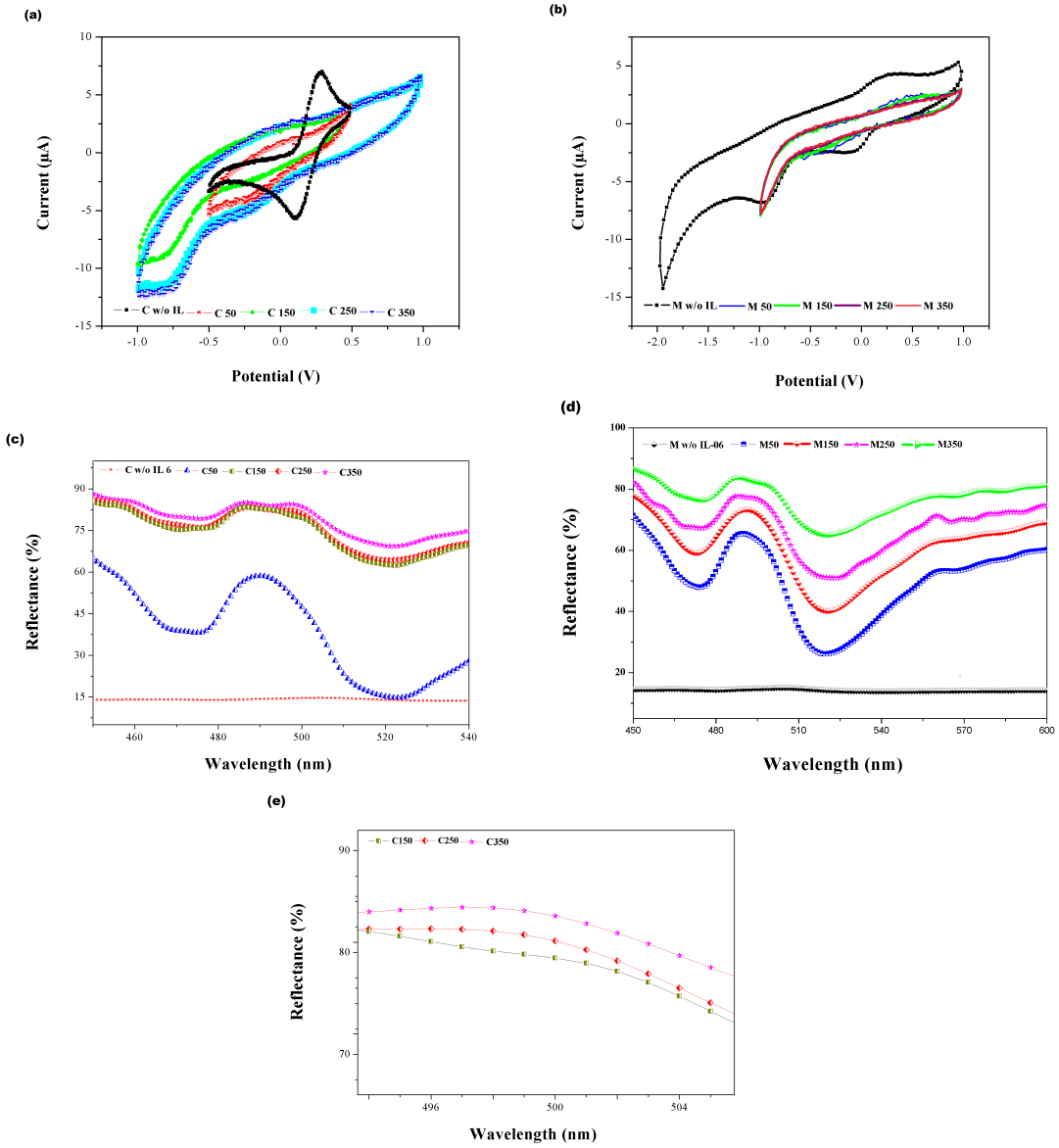

Fig. 7 MPC based Immunoassay. Cyclic voltammetry of (a) CoF based MPC (b) Magnetite based MPC before and after incubation with IL-6 of concentrations 50, 150, 250, 350 pg/ml. Recorded with E_{range}= -2.5 to +2.5 V; ν = 50 mV/s in 0.001M $K_3Fe(CN)_6$. Reflectance spectra of (c) CoF- MPC and (d) Magnetite-MPC following incubation with IL-6 (50, 150, 250 & 350 pg/ml).(e) A closer display of CoF-MPC based reflectance spectra indicating shift from λ_{491} to λ_{498} and increase in reflectance intensity at higher concentrations of IL-6.

CV plot in figure 7 b elaborates a quasi reversible electrode reaction. However the analyte binding process completely blocks its current carrying capacity and both I_{pa} & I_{pc} disappeared. Decreasing current response is consistent with the findings of Eissa et al. & Molazemhosseini et al. who developed electrochemical immunosensor for the quantitative detection of HbA1c and Okadaic acid[37,38]. The antigen-antibody complex formed at the electrode interface, offers increased charge transfer resistance to the diffusing ionic species of redox probe.

Figure 8 c & D demonstrates a linear relation between change in d-spacing/ $\triangle R\%$ with increasing concentration of IL-6. Using Bragg relation, d-spacing was calculated at normal incidence, refer to equation 1 & 2.

$$\lambda = 2d\eta sin\theta, \tag{1}$$

$$\triangle d_{Bragg} = \triangle\lambda_{Bragg}/2*\Delta\eta_t, \tag{2}$$

Where,

$$\Delta\eta_t = \eta_{cg} - \eta_{mpc} \tag{3}$$

The expression $\Delta\eta_t$ in 3 represents the change in refractive index following analyte binding step. It is calculated as difference between refractive indices of chitosan-gelatin hydrogel/η_{cg} and MPC sensor (η_{mpc}) with bound IL-6 as shown in equation 3. Magnetite-MPC as discussed earlier shows a strong linear re-

View Article Online
DOI: 10.1039/D0NR01151G

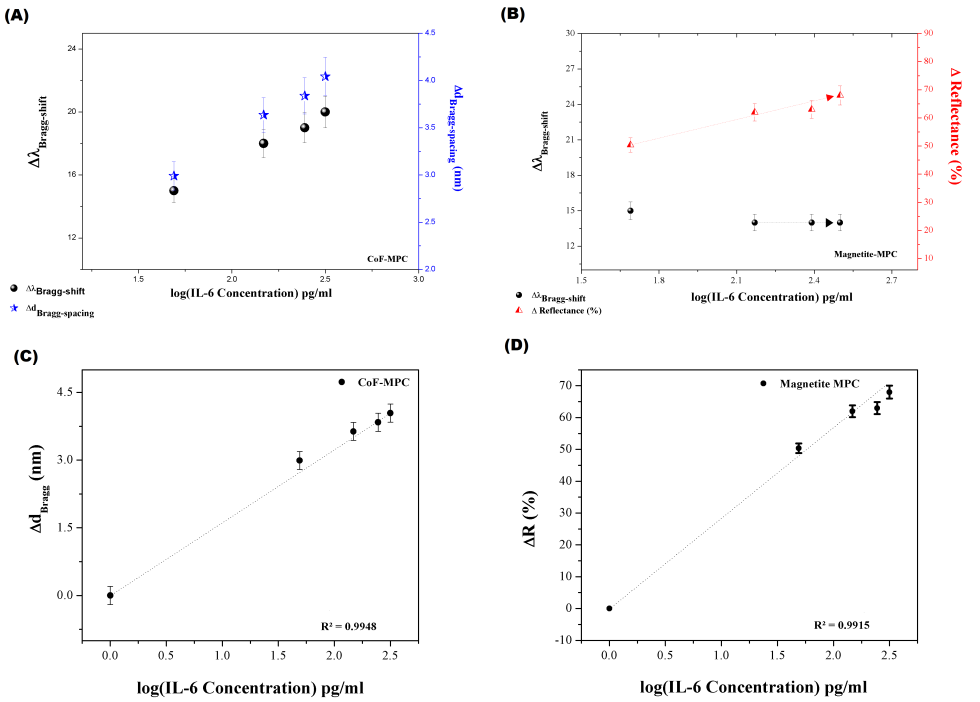

Fig. 8 Calibration Curve. (A) CoF-MPC shows linearity with $\Delta\lambda_{Bragg}$ as well as d_{Bragg} spacing. (B) Magnetite-MPC exhibits strong correlation with only ΔR (%) while $\Delta\lambda_{Bragg}$ becomes constant at higher concentrations. (C) CoF-MPC Sensor shows linear relation with λ_{Bragg} and d_{Bragg} spacing. Regression analysis shows a strong linear relation with R^2=0.9948. (D) Magnetite-MPC sensor shows linear response to Δ R (%) at higher concentrations, R^2=0.9915.

lation with change in reflectance, see figure 8B. The band-shift ceases and becomes constant at 492 nm and it can be ascribed to the resulting steric and charge stabilization following adsorption of analyte on the surface of magnetite based sensor. As a consequence, the change in reflectance was a function of analyte concentration and it is found to be partially dependent on change in Bragg-spacing of PC.

A comparison of performance between two MPCs in quantitative analysis, reveals that a more consistent linear response is obtained in the CoF based design however spectral resolution can be improved by attuning the size of nanospheres[25]. Figure 8 A & B show difference in properties of the CoF and Magnetite MPC sensors. From reflectance spectra, we computed refractive indices at respective concentrations using relation mentioned in equation 4. Bragg's relation shown in equations 1 & 2 was used to compute change in d-spacing which is the inter-particle distance of MNS arranged as 3D colloid in hydrogel matrix. When optical response is plotted against IL-6 concentrations in case of Magnetite MPC sensor, we observed that the lattice spacing stopped increasing at higher concentrations and change in reflectance (%) (figure 8B) showed strong linear correlation with analyte concentration (figure 8D). In contrast, CoF based MPC showed linear response to both $\Delta\lambda_{Bragg}$ as well as Δd_{Bragg} spacing to varying concentration of IL-6, refer to figure 8 A and D.

The calculated limit of detection/LOD[39] for CoF-MPC was 0.52 pg/ml while limit of quantification/LOQ was 1.7 pg/ml. Signal-to-noise (S/N) ratio was higher in Magnetite-MPC with lower limits of detection and quantification. Table 2 elaborates sensor's characteristics which are calculated from reflectance spectra and respective resonant wavelengths. Interestingly, Magnetite based MPC sensor showed linear response only with ΔR% and shift in Bragg's spacing remains unchanged at higher concentration, see supplementary figure 4 B. This difference in sensor's response can be ascribed to the steric or charge stabilization process following antigen-antibody complex formation which might have prevented further shift in *d*-spacing of the Magnetite-MPC crystal. Here, it is worth noting that higher SNR (2.28) for Magnetite based detection mechanism imply formation of stable colloidal array compared to MPC sensor fabricated using CoF MNS with S/N ratio 2.15. The quantitative analysis for detection of interleukin 6 was performed under similar physiological conditions for both types of sensors.

Recently, an invasive electrochemical sensor was developed for real time monitoring of IL-6[4] and an array of disc shaped microelectrodes made of gold were fabricated on a needle substrate. The iR drop and noise was significantly reduced in this method but it exhibits a narrow dynamic range due to the small surface area. Few other non-invasive approaches based on the similar principle were developed for POC devices and wearable technologies which are still in its nascency[5,40]. In comparison to it, label free detection of interleukin-6 through MPC-hydrogel offers a non-invasive & more rational approach for the development of embedded sensor system thus enabling one to use sensors output as control signal for integrated drug delivery mechanism.

Some limitations of the previously developed photonic crystal based sensing mechanisms are poor spectral resolution and

View Article Online
DOI: 10.1039/D0NR01151G

higher limits of detection which hindered its implementation in POC devices. Choi *et al.* [14] developed a hydrogel based PC with an inverse opal structure to detect human IgG and he reported a band-shift of 50 nm at a concentration of 10 mg/ml. With the use of magnetic photonic crystal, we achieved tremendous improvement in limit of detection and the tested dynamic range (50-350 pg/ml) falls within the prognostic levels (90-502 pg/ml) of interleukin 6 for sepsis[41]. Our findings suggest that incorporation of magnetic nanomaterials for development of 3D colloidal PC greatly enhances the S/N ratio but also reduces the limit of detection, refer to table 2.

3.4 Negative Refraction

We also investigated change in refractive properties of the MPC at interface in response to increasing concentration of analyte. Using relation mentioned in equation 4, refractive indices were calculated for respective concentrations of interleukin 6[42]. It is evident from plot 9 a & b, that as-synthesized 3D colloidal magneto-photonic crystal is left-handed and negatively refracts incident light.

$$n_f = \frac{1+R+\sqrt{R}}{1-R}, \tag{4}$$

$$n^2(\omega) = \varepsilon(\omega)\,\mu(\omega), \tag{5}$$

Dielectric nanostructures with higher refractive index when arranged periodically at sub-wavelength spacing in a lower refractive index medium, refracts light in the plane of incident light and it's primarily due to the complex Bragg scattering[43]. In negative refractive media, the Poynting vector and wave vector are anti-parallel to each other which results in phase propagation in the opposite direction[44].

Refractive index is a frequency dependent function of permitivity and permeability, refer to equation 5. Another way to explain negative refraction is that resonance associated to the aforementioned depending parameters are anti-parallel to each other & the effective index is shifted to opposite direction[25].
To validate the observed negative refraction by constituent magnetic nanospheres based MPC, we implemented Finite Difference Time Domain (FDTD) method on a 3D model of magnetic colloidal array using Optiwave Software. FDTD solves Maxwell's Curl equation in time domain using Yee Algorithm[45]. Photonic device was modeled in x-z plane and propagating wave traveled in z-direction. Energy distribution is plotted by software at infinite xy-plane. Simulation of three dimensional photonic device is performed in a cubic mesh also known as Yee Space Lattice and field components ($E_{y,i,j,k}$;$H_{y,i,j,k}$) are positioned at edges orthogonal to each other[45]. Equations 6 & 7 explain implementation of Yee algorithm to compute electric and magnetic componets as a function of permitivity (ε) and magnetic permeability (μ).

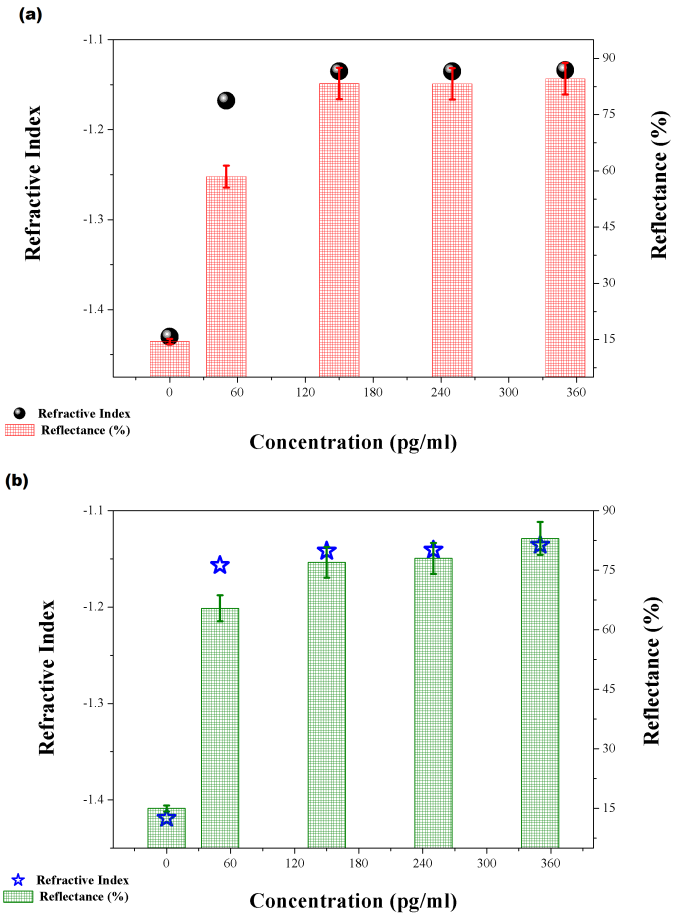

Fig. 9 Negative Refraction by MPC-Hydrogel. Refractive index calculated from Stoke's optical treatment formula shows that synthesized MPC-Hydrogel behaved as Left Handed Material (a) CoF-MPC Sensor (b) Magnetite-MPC sensor and it shows increasing trend at higher concentrations of IL-6 except of Magnetite-MPC at 250 pg/mL.

Table 2 Calculated properties of magneto-photonic sensor.

Type	LOD †	LOQ †	Sensitivity	S/N ratio
Cobalt Ferrite	0.52	1.7	0.5⋆	2.15
Magnetite	0.08	0.2	27.1‡	2.28

† LOD & LOQ are mentioned in pg/ml
⋆ mentioned in nm/pgml^{-1}
‡ mentioned in a.u/pgml^{-1}.

$$H^{n+1/2}_{y,i-1/2,j,k-1/2} = H^{n-1/2}_{y,i,j-1/2,k-1/2} + \frac{\Delta t}{\mu_0 \Delta x}\left(H^{n}_{z,i,j,k-1/2} - H^{n}_{z,i-1/2,j,k-1/2}\right) - \frac{\Delta t}{\mu_0 \Delta z}\left(H^{n}_{x,i-1/2,j,k} - E^{n}_{x,i-1/2,j,k-1/2}\right) \tag{6}$$

View Article Online
DOI: 10.1039/D0NR01151G

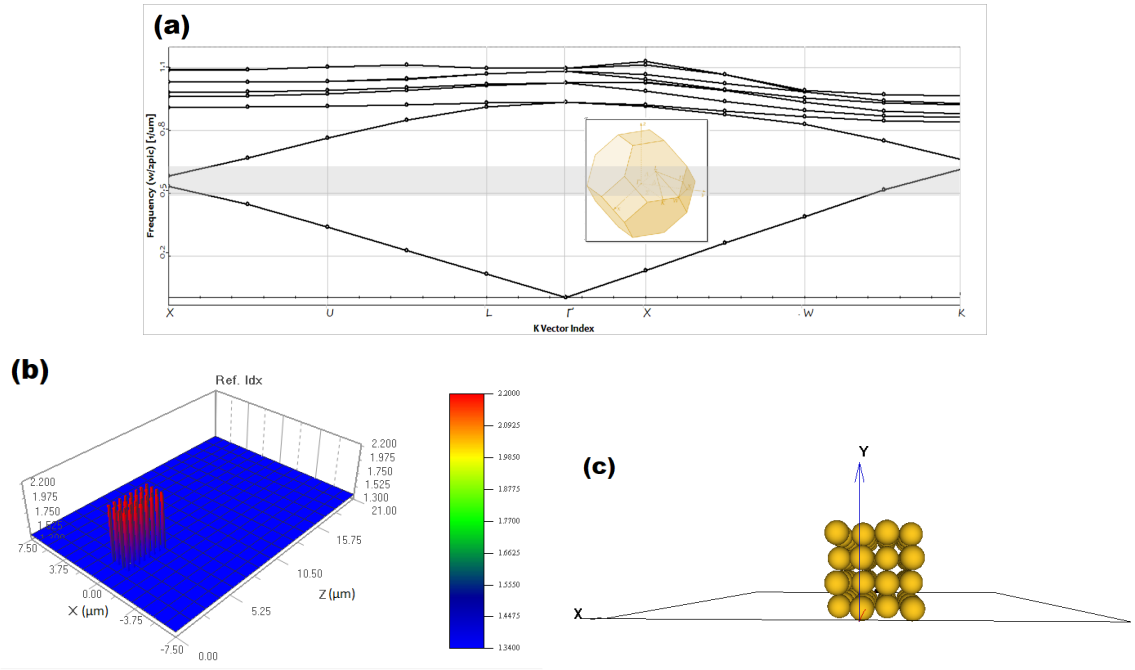

Fig. 10 Simulation of Magneto-Photonic Crystal.(a) Photonic bandgap diagram of Magnetite-MPC (b) Refractive index distribution of MPC (c) 3D simulated self-assembled *fcc* MPC.

$$E^{n+1}_{y,i,j-1/2,k} = \frac{2\varepsilon - \sigma\Delta t}{2\varepsilon + \sigma\Delta t} E^{n}_{y,i,j-1/2,k} + \frac{2\Delta t}{(2\varepsilon + \sigma\Delta t)\Delta z}\left(E^{n+1/2}_{x,i,j-1/2,k+1/2} - E^{n+1/2}_{x,i,j-1/2,k-1/2}\right) - \frac{2\Delta t}{2\varepsilon + \sigma\Delta t}\left(E^{n+1/2}_{z,i,j-1/2,k+1/2} - E^{n+1/2}_{z,i,j-1/2,k-1/2}\right) \quad (7)$$

The accuracy of used method is dependent on space and time steps. Space step is determined from minimum wavelength and maximum refractive index($minimum(\Delta x, \Delta y, \Delta z) \leq \frac{\lambda_{min}}{10 n_{max}}$) & time step for three dimensional system. The latter is calculated using relation $\Delta t \leq \frac{1}{\upsilon\sqrt{\frac{1}{(\Delta x)^2}+\frac{1}{(\Delta y)^2}+\frac{1}{(\Delta z)^2}}}$ whereas υ is velocity of light.

Figure 10 b shows a three dimensional model and the refractive index of MNS was set as 2.2[46] and 1.34 for medium enclosing it[47]. Wafer dimension was set as 21×8 μm. Gaussian modulated continuous wave with λ =1.5 μm was used as input wave with a time offset and half-width of 4.5e-014 seconds and 1.5e-014 seconds respectively. The mesh size of simulation domain was set as 0.05 μm and anisotropic perfectly matched layer (APML) boundary conditions were used to compute E_y and H_y distributions with time step size of 8.339 sec. Amplitude and phase information of propagating wave are obtained from Fourier Transform complex field components and it also helps analyze the refractive properties of devised photonic system. To generate band diagram of designed MPC, we used *K*-vector path of truncated octahedron because the self-assembled array has face centered cubic *(fcc)* lattice. A three dimensional band solver was used with hybrid polarization and mesh size of $16\times16\times16$ to compute bands. Figure 10a and c demonstrate photonic band diagram and distribution of refractive index respectively. A partial or pseudo-gap at symmetry point *X* and *K* can be observed which corresponds to the reflecting wavelength shown in figure 4 d & e. Our findings are consistent with band diagram of *fcc* dielectric sphere lattice which are reported in earlier studies. The field distribution plots of magnetic (H_y) and electric (E_y) components of propagating wave were analyzed to understand the dispersion phenomenon occurring at the interface of two different dielectric media, refer to figures 11 & 12. There is a concentric distribution of amplitude, imaginary and real components of (E_y), see figures 11 b, d and 12 b. It should also be noted that E_y phase (positive) and power (negative) have opposite directions (figure 12 a and b) which as explained by Veselago (2006), are negatively refractive materials[48]. On the contrary, H_y shows a nodal distribution of amplitude, real and imaginary parts of field at the edges of colloidal array, see figures 11a, c & 12a. The magnetic field is highest around the edges of lattice and ceases to propagate as it encounters the colloidal array. This resulted in zero power distribution in xy-plane. Figure 12a shows comparison of phase power with imaginary field distribution plot of H_y component.

The features of nanostructure intended for PC fabrication such as size, shape, separation and spatial arrangement can be used as control factors to attune the magneto-optical properties of the resultant super-lattice that exhibits photonic confinement over a wider visible range. Periodic inter-particle spacing with sub-wavelength orders of magnitude, requires high colloidal stability in the selected media. Self-assembly of magnetic nanospheres in aqueous media is primarily due to the dominating electrostatic repulsion between highly charged particles for instance in case of superparamagnetic magnetite when exposed to external mag-

View Article Online
DOI: 10.1039/D0NR01151G

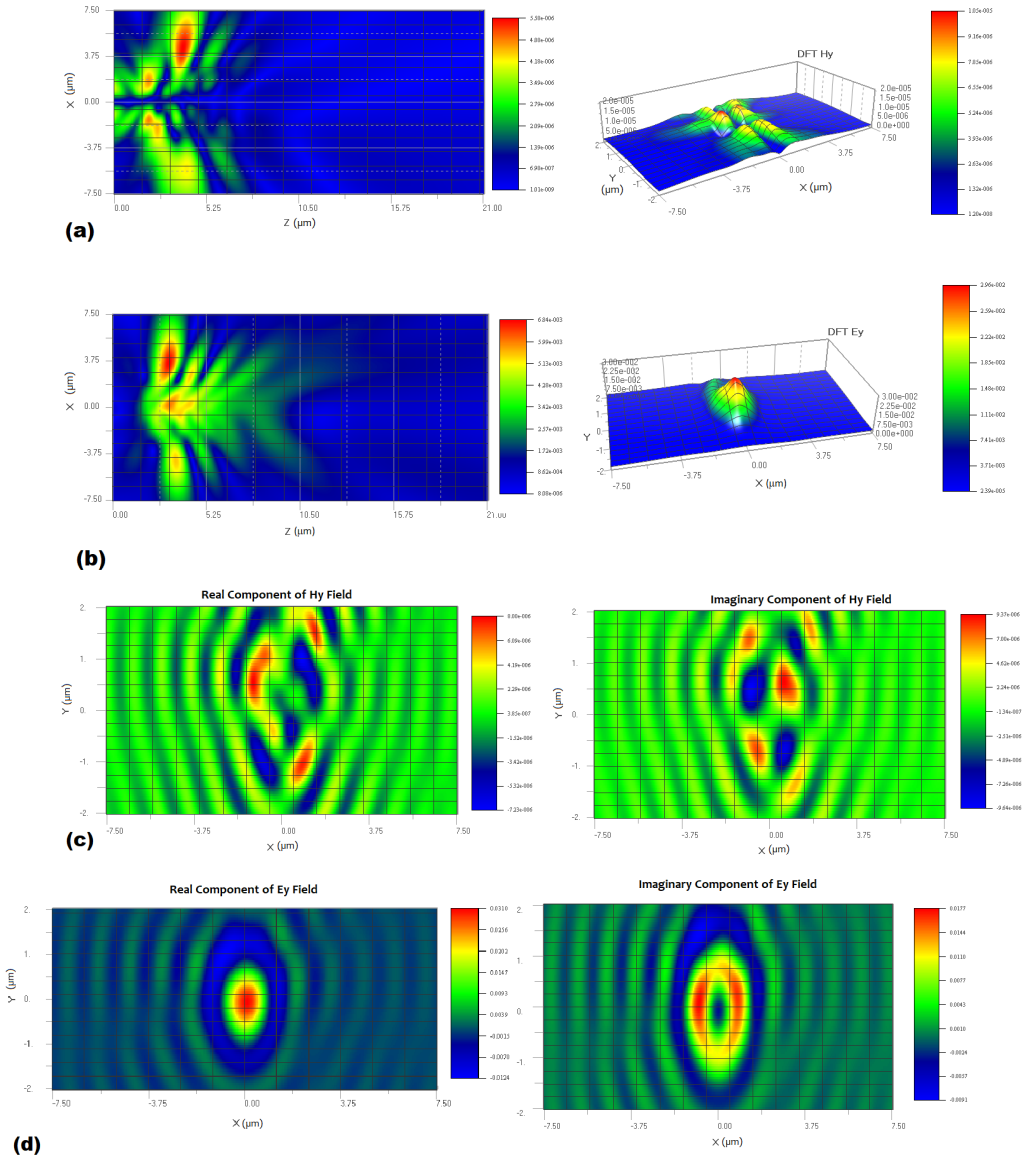

Fig. 11 Electromagnetic field distribution plots of designed MPC. (a) Amplitude of H_y field in X-Z (left) X-Y (right) planes. (b) Amplitude of E_y field in X-Z (left) X-Y (right) planes. (c) Real (left)and complex (right) components of H_y field of propagating wave. (d) Real (left)and complex (right) components of E_y field of propagating wave.

netic field[36]. In this work, we chose chitosan-gelatin hydrogel in aqueous solution with slightly acidic pH thereby maintaining positive charges on polymer which is expected to facilitate self-assembly of magnetic nanospheres carrying net positive charge inside the matrix. We designed this biosensing platform particularly for real-time sepsis management in patients of higher degree burns. Koskela *et al.* mentions sepsis associated high levels of interleukin-6 in blister fluid of burn patients with prognostic range of 23-203 pg/ml which falls within reported dynamic range of MPC biosensor. Application of an intelligent hydrogel with integrated MPC biosensor on burn wounds allows on-site detection of sepsis using a hand-held spectrum analyzer. However, the interesting left handed nature of such photonic crystal makes them an attractive candidate for magneto-inductive lens in magneto-resonance imaging (MRI)[49,50],

4 Conclusion

A major challenge that emerging health care diagnostic technologies particularly point-of-care & wearable devices are facing now-a-days is accurate quantitative analysis of physiological parameters within a complex biochemical environment. Such devices usually employ electrochemical transducers to quantify diagnostic proteins because it's a well-established method that allows fabrication of miniaturized devices. The ratio of signal to least detectable concentration is very low due to the nature of sensor's architecture and this limits its application in the detection of cancer biomarkers which are present in blood with lower concentrations normally in the range of pg/mL. Additionally, the reported designs of electrochemical biosensor do not facilitate integration with a therapeutic mechanism. Here, we reported an embedded magneto-photonic crystal based detection mechanism

View Article Online
DOI: 10.1039/D0NR01151G

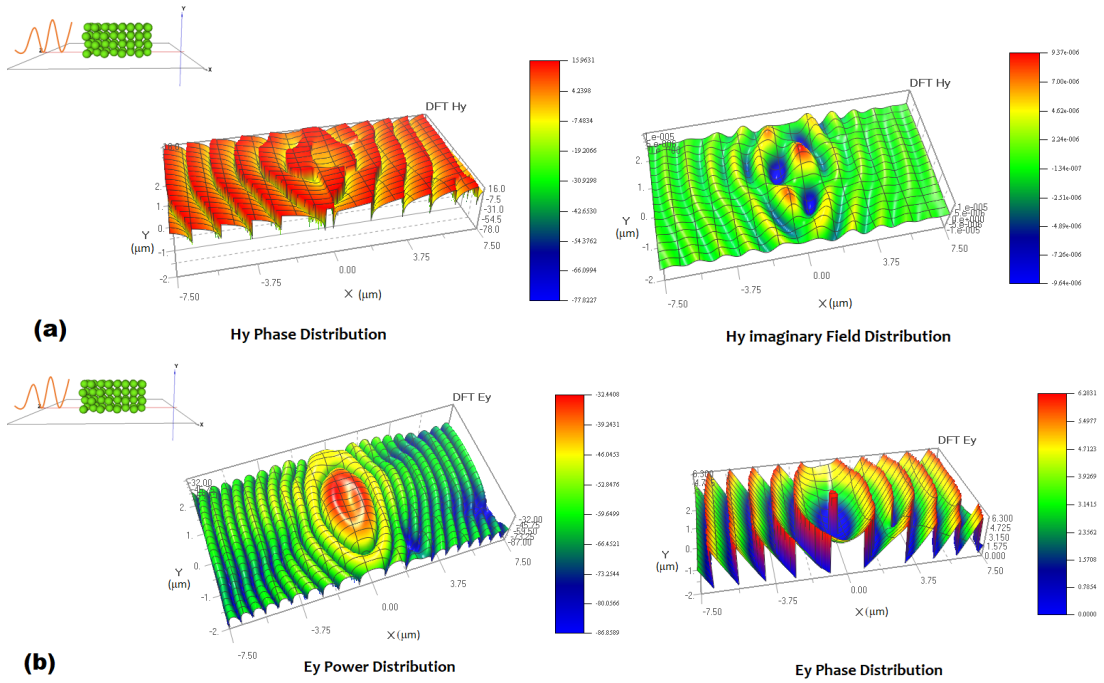

Fig. 12 Negative refraction; an implicit function of inverse phase and power relation. (a) *(left)* Phase distribution of Magnetic field component *(right)* Complex Power of magnetic field component if propagating wave. (b)*(left)* Power & *(right)* phase of Ey field.

for Interleukin 6 which is an extensively studied biomarker for sepsis and cancer diagnosis. We exploited light reflecting properties of the 3D colloidal MPC assembled inside a hydrogel matrix to detect IL-6 bound on the surface of bioconjugated magnetic nanospheres. The findings of reflectance spectroscopy indicate it is highly sensitive to the interfacial immune reactions. The resonant wavelength undergoes blue-shift as the target binds to detecting antibody immobilized on nanospheres and it also causes a sharp increase in reflectance intensity. At a concentration of 50 pg/mL, the CoF and Magnetite based MPC sensors show 44% & 50% increase in reflectance intensity respectively. Supplementary figures 15 & 13 show the flexibility and biocompatibility of the developed MPC hydrogel. The integrated mechanism presented in this study, can be a promising approach for real time management of sepsis in higher degree burns or cancer treatment.

Conflicts of interest

"The authors of this study declare no conflict of interest.".

Acknowledgements

This study was sponsored by Higher Education Commission(HEC) of Pakistan and completed in collaboration with Nanyang Technological University, Singapore. The authors thank W. Manalastas, M. Sirnivasan for providing us electrochemical characterization facility & S.N. Arshad from Lahore University of Management Sciences, Pakistan for sharing Scanning Electron Microscopy facility. We also thank W. Poh for his assistance in cell viability assay.

Data Availability

The supporting data can be provided upon reasonable request from the corresponding author.

Notes and references

1 M. Toma and K. Tawa, *ACS applied materials & interfaces*, 2016, **8**, 22032–22038.
2 P. Buchegger, U. Sauer, H. Toth-Székély and C. Preininger, *Sensors*, 2012, **12**, 1494–1508.
3 R. Kapoor and C.-W. Wang, *Biosensors and Bioelectronics*, 2009, **24**, 2696–2701.
4 C. Russell, A. C. Ward, V. Vezza, P. Hoskisson, D. Alcorn, D. P. Steenson and D. K. Corrigan, *Biosensors and Bioelectronics*, 2019, **126**, 806–814.
5 M. Tertiş, B. Ciui, M. Suciu, R. Săndulescu and C. Cristea, *Electrochimica Acta*, 2017, **258**, 1208–1218.
6 T. Yang, S. Wang, H. Jin, W. Bao, S. Huang and J. Wang, *Sensors and Actuators B: Chemical*, 2013, **178**, 310–315.
7 G.-C. Fan, X.-L. Ren, C. Zhu, J.-R. Zhang and J.-J. Zhu, *Biosensors and Bioelectronics*, 2014, **59**, 45–53.
8 K. Zhang, G. Liu and E. M. Goldys, *Biosensors and Bioelectronics*, 2018, **102**, 80–86.
9 Y. Lou, T. He, F. Jiang, J.-J. Shi and J.-J. Zhu, *Talanta*, 2014, **122**, 135–139.
10 T. Kishimoto and T. Tanaka, *Encyclopedia of Inflammatory Diseases*, 2015, 1–8.
11 J. Bauer and F. Herrmann, *Annals of hematology*, 1991, **62**, 203–210.
12 I. Ndede, S. K. Mining, K. Patel, F. M. Wanjala, D. Chumba

View Article Online
DOI: 10.1039/D0NR01151G

and C. Tenge, *BMC research notes*, 2017, **10**, 519.
13 V. W.-S. Wong, J. Yu, A. S.-L. Cheng, G. L.-H. Wong, H.-Y. Chan, E. S.-H. Chu, E. K.-O. Ng, F. K.-L. Chan, J. J.-Y. Sung and H. L.-Y. Chan, *International journal of cancer*, 2009, **124**, 2766–2770.
14 E. Choi, Y. Choi, Y. H. P. Nejad, K. Shin and J. Park, *Sensors and Actuators B: Chemical*, 2013, **180**, 107–113.
15 Y. Wang, C.-J. Huang, U. Jonas, T. Wei, J. Dostalek and W. Knoll, *Biosensors and Bioelectronics*, 2010, **25**, 1663–1668.
16 J. D. Joannopoulos, S. G. Johnson, J. N. Winn and R. D. Meade, *Princeton Univ. Press, Princeton, NJ [ua]*, 2008.
17 A. C. Sharma, T. Jana, R. Kesavamoorthy, L. Shi, M. A. Virji, D. N. Finegold and S. A. Asher, *Journal of the American Chemical Society*, 2004, **126**, 2971–2977.
18 K. A. Kilian, L. M. Lai, A. Magenau, S. â. n. Cartland, T. Bocking, N. Di Girolamo, M. Gal, K. Gaus and J. J. Gooding, *Nano letters*, 2009, **9**, 2021–2025.
19 D. Gallegos, K. D. Long, H. Yu, P. P. Clark, Y. Lin, S. George, P. Nath and B. T. Cunningham, *Lab on a Chip*, 2013, **13**, 2124–2132.
20 K. Hayashi, M. Nakamura, W. Sakamoto, T. Yogo, H. Miki, S. Ozaki, M. Abe, T. Matsumoto and K. Ishimura, *Theranostics*, 2013, **3**, 366.
21 J. Ge, Y. Hu, M. Biasini, W. P. Beyermann and Y. Yin, *Angewandte Chemie International Edition*, 2007, **46**, 4342–4345.
22 K. Petcharoen and A. Sirivat, *Materials Science and Engineering: B*, 2012, **177**, 421–427.
23 M. A. Khan, M. Mujahid, I. Gul and A. Hussain, *Electrochimica Acta*, 2019, **295**, 113–123.
24 J. Fouineau, K. Brymora, L. Ourry, F. Mammeri, N. Yaacoub, F. Calvayrac, S. Ammar-Merah and J.-M. Greneche, *The Journal of Physical Chemistry C*, 2013, **117**, 14295–14302.
25 H. Alaeian and J. A. Dionne, *Optics express*, 2012, **20**, 15781–15796.
26 R. E. Rosensweig, *Journal of magnetism and magnetic materials*, 2002, **252**, 370–374.
27 J.-P. Fortin, C. Wilhelm, J. Servais, C. Ménager, J.-C. Bacri and F. Gazeau, *Journal of the American Chemical Society*, 2007, **129**, 2628–2635.
28 W. Somers, M. Stahl and J. S. Seehra, *The EMBO journal*, 1997, **16**, 989–997.
29 C. Blanchetot, N. De Jonge, A. Desmyter, N. Ongenae, E. Hofman, A. Klarenbeek, A. Sadi, A. Hultberg, A. Kretz-Rommel, S. Spinelli *et al.*, *Journal of Biological Chemistry*, 2016, **291**, 13846–13854.
30 J. B. Wood, M. W. Szyndler, A. R. Halpern, K. Cho and R. M. Corn, *Langmuir*, 2013, **29**, 10868–10873.
31 M. E. Lynge, R. van der Westen, A. Postma and B. Städler, *Nanoscale*, 2011, **3**, 4916–4928.
32 G. Loget, J. B. Wood, K. Cho, A. R. Halpern and R. M. Corn, *Analytical chemistry*, 2013, **85**, 9991–9995.
33 S. Shi, L. Wang, R. Su, B. Liu, R. Huang, W. Qi and Z. He, *Biosensors and Bioelectronics*, 2015, **74**, 454–460.
34 J. Huang, J. Harvey, W. D. Fam, M. A. Nimmo and I. A. Tok, *Procedia Engineering*, 2013, **60**, 195–200.
35 S. Akira, T. Taga and T. Kishimoto, *Advances in immunology*, Elsevier, 1993, vol. 54, pp. 1–78.
36 J. Ge and Y. Yin, *Advanced materials*, 2008, **20**, 3485–3491.
37 S. Eissa and M. Zourob, *Nanoscale*, 2012, **4**, 7593–7599.
38 A. Molazemhosseini, L. Magagnin, P. Vena and C.-C. Liu, *Sensors*, 2016, **16**, 1024.
39 J. Miller and J. C. Miller, *Statistics and chemometrics for analytical chemistry*, Pearson education, 2018.
40 H. Chen, T. K. Choo, J. Huang, Y. Wang, Y. Liu, M. Platt, A. Palaniappan, B. Liedberg and A. I. Y. Tok, *Materials & Design*, 2016, **90**, 852–857.
41 M. Koskela, T. Ala-Kokko, F. Gäddnäs, K.-H. Herzig, T. Karhu, A. Oikarinen and V. Koivukangas, *Acta Anaesthesiologica Scandinavica*, 2017, **61**, 53–61.
42 M. Born and E. Wolf, *Principles of optics: electromagnetic theory of propagation, interference and diffraction of light*, Elsevier, 2013.
43 V. F. Chernow, R. C. Ng and J. R. Greer, Photonic and Phononic Properties of Engineered Nanostructures VII, 2017, p. 101120G.
44 F. Ouerghi, F. AbdelMalek, S. Haxha, R. Abid, H. Mejatty and I. Dayoub, *Journal of lightwave technology*, 2009, **27**, 3269–3274.
45 S. D. Gedney, *Synthesis Lectures on Computational Electromagnetics*, 2011, **6**, 1–250.
46 G. Tao, W. Xin, W. Yan and D. Xiang-Mei, *Chinese Physics B*, 2015, **24**, 124208.
47 K. Basavaraju, T. Damappa and S. Rai, *Carbohydrate polymers*, 2006, **66**, 357–362.
48 V. Veselago, L. Braginsky, V. Shklover and C. Hafner, *Journal of Computational and Theoretical Nanoscience*, 2006, **3**, 189–218.
49 S. B. Yeap, X. Qing and Z. N. Chen, 2016 International Workshop on Antenna Technology (iWAT), 2016, pp. 138–141.
50 R. Schmidt, A. Slobozhanyuk, P. Belov and A. Webb, *Scientific reports*, 2017, **7**, 1678.

Supplementary Information

- Figure13:MPC Hydrogel Flexibility.
- Figure14:Cyclic Voltammetry of unconjugated CoFMPC.
- Figure15:Cell Viability Assay.

Flexibility

We folded MPC-Hydrogel at 180° to confirm if it can conform with contouring surface when used as dressing. Figure 13 shows its flexible nature.

View Article Online
DOI: 10.1039/D0NR01151G

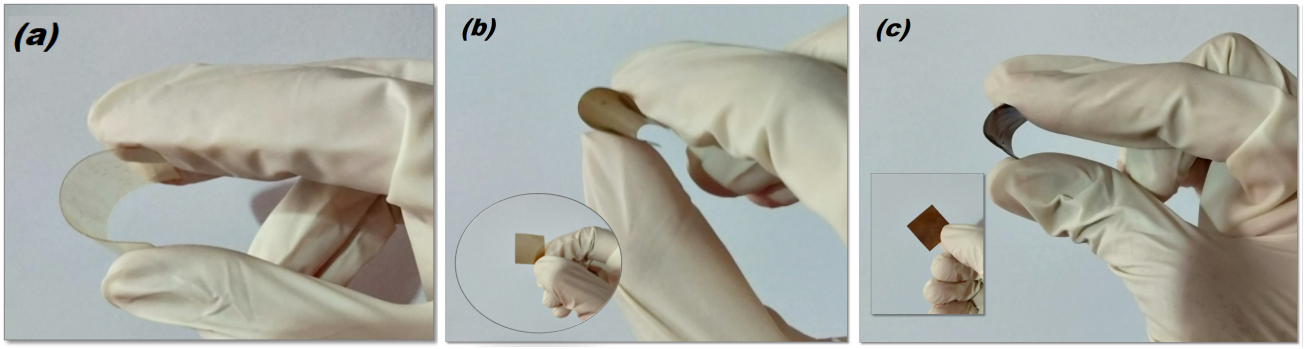

Fig. 13 MPC Hydrogel. Flexibility of synthesized MPC when folded at 180°. (*a*) Hydrogel made of chitosan-gelatin (CG) with 1:5 ratio. (*b*) CG-CoF (0.05% w/v) MPC Hydrogel with embedded IL-6 Sensor is more flexible and easily bendable. (*c*) CG-CoF (0.1% w/v) MPC Hydrogel with embedded IL-6 Sensor offers resistance and has some rigidity when folded.

Cell Viability Assay

We performed cytoxicity assay using PrestoBlue to evaluate if increasing concentration of MNS negatively influence the growth of human dermal cell. Human Dermal Fibroblast cells/HDF were grown and passaged in DMEM media containing 10% FBS and Penicillin antibiotic with a seeding density of 2.4×10^6 cells in a T75 flask. In 96-wells microplate, three different hydrogel samples (0.05%, 0.1% Magnetic and plain Chitosan-Gelatin Hydrogel) of similar size and dimensions were placed and 648 μL of media containing 1.4×10^4 cells were dispensed in each well. The cells were left inside CO_2 (Sanyo CO_2 Incubator) at 37 °C for 24 hours. Next day, we incubated the cells grown over hydrogel after PrestoBlue addition for an hour and measured absorbance at 570 and 600 nm. After measurement, media was changed and cells were kept again on incubation for another 24 hours. Each hydrogel sample was run in duplicate with n=4. The untreated cells exhibited 100% viability and was used as reference for comparison. One-way ANOVA was performed to determine effect of MNS concentration on the HDF growth. Concentration dependent viability test was performed only for CoF based MPC. The treated cells were grown at 0.05% and 0.1 % MPC hydrogel (labeled Magnetic Gel) and following 48 hours, cells grown over 0.1% MPC-Hydrogel showed highest viability percentage, refer to figure 15.

View Article Online
DOI: 10.1039/D0NR01151G

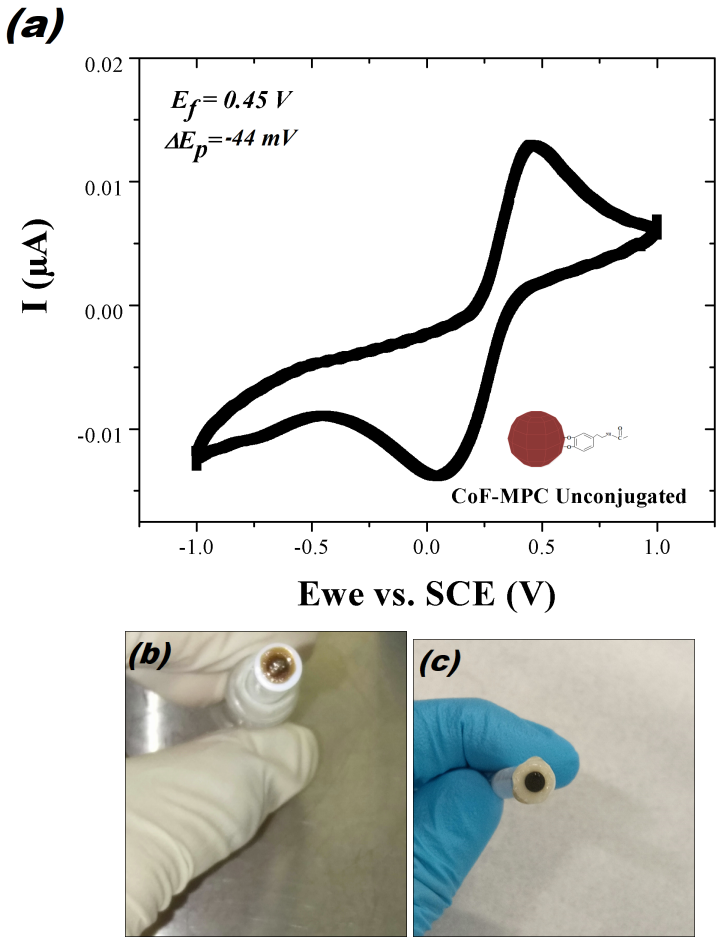

Fig. 14 CV of unconjugated CoF MPC. (a) Cyclic voltammetry of GCE coated with Cobalt Ferrite nanocomposite with chitosan-gelatin hydrogel. It was recorded at E_{range}= -2.5 to +2.5 V; v = 50 mV/s in 0.001M $K_3Fe(CN)_6$ [23]. (b) GCE coated with conjugated Cobalt Ferrite magneto-photonic crystal. (c) CoF-MPC coated electrode following incubation with IL-6 and subsequent CV recording. The MPC-hydrogel did not detach but doubled its size after consecutive readings.

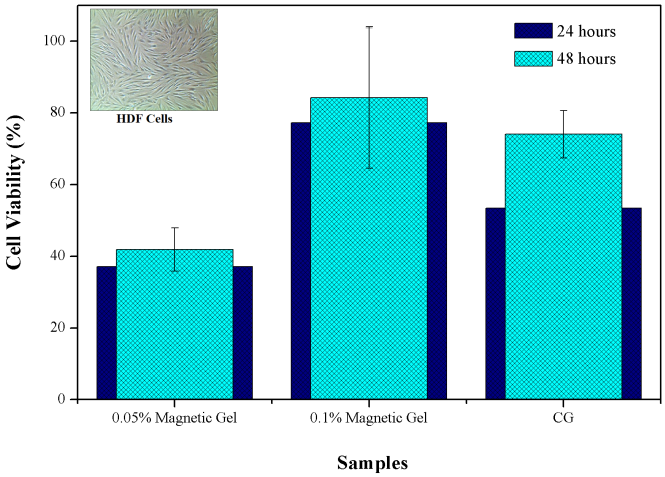

Fig. 15 Cytotoxicity Assay. Human Dermal Fibroblast grown over Chitosan-Gelatin, MPC-Hydrogel 0.05% & 0.1% were tested for cytotoxicity after 24 and 48 hours, using PrestoBlue assay. At α=0.05, the population variations & means are significantly different.